# H-Man: Characterization of a Novel, Portable, Inexpensive Planar Robot for Arm Rehabilitation

Paolo Tommasino, Lorenzo Masia, Welihena GKC Gamage, Azhar Muhammad,
Charmayne ML Hughes and Domenico Campolo

*Abstract*— **In the past decades there has been an increasing interest in the design of robotic platforms suitable to assist the conventional motor therapy and/or to study human motor control. Most of the proposed solutions, however, come with intrinsic limitations that in turn limit the final use of the device itself. For instance, encumbrance, sophisticated control architectures and high costs translate into cumbersome and expensive devices whose diffusion is still limited to laboratories and specialized clinical settings. This paper presents a novel, two degrees-of-freedom planar device conceived according to three main principles: *portablility*, *cost-effectiveness* and *ease of control*. The key ingredient of the device is a planar *H-shaped cable differential mechanism* which ensures a constant Jacobian and a homogeneous perceived inertia over the entire workspace. The paper presents the mechanical design as well as the performance evaluation in terms of bandwidth, Z-width and perceived impedance.**

## I. INTRODUCTION

Recent advances in mechatronics and system control made 'haptic displays' possible to render tactile information (haptics) in response to users motion, hence extending the human-machine-interaction experience with the additional *sensation* of touch[1]. Haptic devices are becoming widespread in different scientific and technological sectors ranging from motor rehabilitation and human motor control[3] to robotic surgery and human-computer interactions[2].

A key concept for a successful haptic interface is its *transparency* or *backdrivability*, i.e. a dynamic mechanical behavior which does not interfere with the user dynamics when moving through free virtual space [4]. System inertia and friction perceived at the contact interface are the parameters which mainly affect the display's transparency.

To increase the backdrivability, haptic devices are often designed with planar linkages and parallelogram-like structures for direct drive transmission [5], [6], [7], [8]. However, such solutions provide a non-homogeneous inertial tensor, i.e. the perceived inertia depends on the robot configuration [21]. In addition, it has been shown that the perceived inertia alters the natural motors strategies, important indicators in the evaluation of motor performance[12], [13]. Whenever homogeneity and high transparency cannot be achieved with the mechanical design, force control techniques can be used to compensate the system dynamics, at least in part [14]. A solution that usually requires additional sensors and sophisticated realtime control, impacting the final cost of the device.

On the other hand, so-called Cartesian robots have been proposed to simplify control. The MEMOS [9] and ARM guide [10] are examples of two planar devices for neuro-rehabilitation of the shoulder/elbow meant to represent a trade-off between the best clinical efficacy and the least amount of robotic complexity.

The ARM guide robot uses a passive, linear constraint with a single motor to assist arm movements and to reduce complexity and costs typical of multi-degrees-of-freedom robots [10]. Unlike the ARM guide, the MEMOS robot is based on a 2D planar mechanism in a Cartesian configuration. While this simplifies the kinematics and therefore the control, the MEMOS robot re-adapts industrial robots design whose position-controlled architectures are not suitable for the flexibility required for interacting with humans. Such a flexibility can be achieved by means of admittance control, whereby force sensors are used to sense the human reaction forces and command appropriate actions. However, this approach has several limitations which impact both the final cost of the device and the computational complexity of the controller.

Unlike conventional machines or robots which are based on complex designs (often readapting industrial mechanisms), this paper presents a novel planar robot that has been conceived to address the aforementioned limitations. High backdrivability and mechanical homogeneity are achieved by minimizing the moving masses and by using a symmetric mechanical design based on a H-shaped cable-driven differential mechanism. The proposed solution makes the H-Man cost-effective, light-weight and easy to control.

## II. THE H-MAN

H-Man consists of the manipulandum, 6 DoF force/torque sensor, 2 DC-motors controlled by a driver and a PC with data acquisition system (possibly scalable down to micro-controller). The force transmission from DC-motors to the manipulandum is carried out through an H-shaped cable-driven mechanism, hence the name H-Man. This configuration, better described below, is a differential mechanism which enables two independent movements in x and y axis despite having just one cable loop. Another major advantage of this differential configuration is that both actuators are grounded hence the subject holding the handle experiences

This work was partly supported by the 'H-Man' project (BMRC-NMRC BnB Grant No. BnB12sep005), Ministry of Health, Singaporea and by the Academic Research Fund (AcRF) Tier1 (RG 50/11), Ministry of Education, Singapore

Authors are with the School of Mechanical and Aerospace Engineering Nanyang Technological University 50 Nanyang Avenue Singapore 639798

E-mail contacts: {paolo001, l.masia, wgkumudu, mazhar, c.hughes, d.campolo}@e.ntu.edu.sg

low inertia. A Cartesian approach in the manipulator is obtained by the linear guides/rails ensuring a homogeneous inertia and friction throughout the whole workspace. This feature is not necessarily available in any robotic manipulandum and non-homogenous impedance might lead to arm trajectories which are curved rather than straight as expected, for example, during reaching tasks. Another significant advantage of having this type of Cartesian differential mechanism is the simplicity of the mechanism resulting in easier control. It will be shown later that the calculations for controlling the mechanism involve only simple algebra without any trigonometric/logarithmic functions or on-line matrix inversions. As a result, a simple microcontroller can execute all the operations in real time, hence reducing the complexity and therefore the cost of the system.

This section describes the working principle of the differential mechanism and its main advantages, followed by the mechanical and electrical parts of the H-Man.

### A. The H-shaped cable-driven differential transmission

A schematic of the H-Man concept is shown in Fig.1 A.

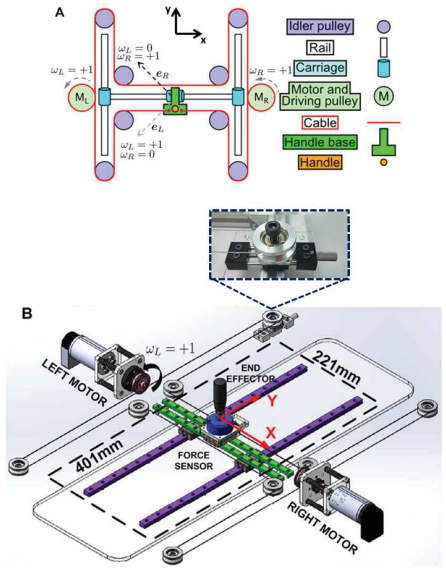


Fig. 1: A) Schematic of the cable-driven differential mechanism. When both motors are actuated with the same speed and rotates in the same direction, the end-effector moves along the $x$ direction. Movements along the $y$ direction are achieved when motors rotate at the same speed but in opposite directions. B) CAD drawing. To avoid slackness, one of the four external idlers is mounted on top of the lead screw guide unit (Misumi XKNEJ20) to enable the manual tuning of the cable pretension

.

The elements $M_L$ and $M_R$ represent pulleys directly connected to the left and right motor (Faulhaber 3863024CR) respectively. The driving pulleys(diameter equal to $27.5mm$) transfer the force to the cable which is routed through 8 idler pulleys(diameter equal to $20.4mm$ ). Ultimately the force is directly transferred to the carriages (and ultimately the handle), with minimal friction losses. The handle is connected rigidly to the horizontal carriage through a solid base.

The parts are arranged to provide planar (i.e. in the xy plane of the table) differential motion. Differential mechanisms are devices that produce resultant motion as sum or difference of the component motions, an example of cabled differential for rotary motions can be found in [19].

In our system, to produce movements in the x axis, $M_L$ and $M_R$ must rotate at the same speed and in the same direction (i.e. either both clockwise or both counter-clockwise), while for that in y axis, in opposite directions. So in Fig.1, both $M_L$ and $M_R$ rotate clockwise to produce movement in positive x direction while, to produce movement in positive y direction, $M_L$ rotates clockwise and $M_R$ rotates anti-clockwise.

For the driving cable, we choose the 0.54 mm nylon coated steel wire rope (7x7) (Asahi Intecc NB45-61). The cable is wrapped 4 turns around the each driving pulley providing a friction that can hold $50N$ force at the manipulator handle when both pulleys are blocked. Note that this last condition guarantees an intrinsic safety requirements. In fact, whenever motor would produce end-effector forces above $50N$ (i.e. in the case of malfunctioning or instability) the cable would slip on the driving pulley hence avoiding the transmission of higher forces at the user's hand.

### B. The Kinematics of the Differential Transmission

Due to the differential transmission and to the mechanical symmetry, end-effector motions of our device can be described with very simple mathematical formula.

In the mechanical assembly and electrical wiring of the robot, our convention is that positive currents induce positive angular velocities with respect to the shaft axis (an axis aligned with the motor shaft and pointing outwards the motor pulley). As shown in Figure 1 (a), this results in two motors' pulling directions ($\boldsymbol{e}_r$ and $\boldsymbol{e}_l$ ) which are orthogonal to each others and are directed along the diagonal of the workspace. This behavior is described by the following kinematic equation:

$$\dot{\boldsymbol{p}} = \begin{bmatrix} \dot{x} \\ \dot{y} \end{bmatrix} = \boldsymbol{J} \begin{bmatrix} \omega_L \\ \omega_R \end{bmatrix} \tag{1}$$

with $\dot{\boldsymbol{p}}$ the velocity vector of the end-effector and $\omega_L$ and $\omega_R$ the angular velocity of the motors.

Note that the Jacobian $\boldsymbol{J}$:

$$\boldsymbol{J} = \frac{r_m}{2} \begin{bmatrix} -1 & -1 \\ -1 & 1 \end{bmatrix} \tag{2}$$

is not configuration-dependent and its definition depends only on the driving pulley radius $r_m$. The column vectors of $J$ corresponds to the motors' pulling directions $e_l$ and $e_r$ represented in Figure 1 (a).

Once the Jacobian has been defined, it can be used to convert the forces $(F_x, F_y)$ acting at the end-effector into the corresponding torques $(\tau_L, \tau_R)$ acting at the motors' shafts:

$$\begin{bmatrix} \tau_L \\ \tau_R \end{bmatrix} = \boldsymbol{J}^T \begin{bmatrix} F_x \\ F_y \end{bmatrix} \quad (3)$$

## III. System Characterization and Performance

In this section we describe the characterization of the device in terms of bandwidth, Z-widths and perceived impedance at the end-effector.

We measured the *bandwidth* of the system in terms of the relationship between the motor current and the forces developed at the end-effector. Such quantity depends upon the performance of every single component, either mechanical (i.e. rigidity, stiction, backlash and so on) or electronic (performance of the servo-drivers and of sensors), that contributes to the force transmission and detection.

The *Z-width* is an important parameter to consider when designing haptic display. It tells the capability of a system to rendering mechanical properties of virtual object such as stiffness (or compliance) and viscosity. It is mainly affected by the sampling frequency of the controller, the sensors resolution and noise and by the saturation of the servo-drivers which in turn limit the stability of the controller[15], [16].

The *perceived impedance* is a measure of the transparency of the system when motors are not actively controlled (passive response). It represents forces delivered by the display's mechanics to the user'hand, hence affecting the way the user can interact with it. Such quantity is important especially for display developed to investigate human motor control or robot for rehabilitation and, if it is not minimal or suitably compensated, it affects the user motor performance [12].

### A. Transmission Bandwidth

Although the majority of the end-effector movements are achieved with both motors active at the same time, here we assume a conservative perspective and evaluate the lower bound of the bandwidth considering the system response due to the control of a single motor.

For finding out the frequency response of the device, a sinusoidal current at different frequencies was commanded to the right motor:$i_c(t) = I_c \sin(2\pi f_0 t)$. The left motor was mechanically blocked to minimize backlash. The end effector was blocked by a custom rigid frame and the force delivered was measured with the force sensor (ATI-Mini 40). Frequency $f_0$ range was chosen between 1-100 Hz, with incremental steps of 1Hz, and amplitude $I_c$ ranging in the set of values $\{0.5\text{A}, 0.75\text{A}, 1\text{A}, 1.5\text{A}\}$. The system was considered at steady state after an initial period of 1 second from the application of the sinusoidal command. The actual currents at the motor,$i_R(f_0, I_c, t)$, as well as the planar force components $F_x^{f_0,I_c}(t), F_y^{f_0,I_c}(t)$ were acquired at a sampling rate of $f_s = 10kHz$ for a number of $N_{cyc}$ cycles (with $N_{cyc} = 10$), for each frequency and for each amplitude. The force components were then combined into planar force vector $\boldsymbol{F}(t)$ and projected along the motor direction $\boldsymbol{e}_r$ to obtain the scalar $F_{e_R}(t)$. Taking advantage of the periodicity of the driving inputs we filter out the noise using a truncated Fourier series expansion. For a generic acquired signal $s(t)$ (either force or current) in response to periodic stimulus, we consider its truncated Fourier series up to the 5th order because we focus on the steady-state response and at the same time we want to take into account system nonlinearities: $\tilde{s}(t) = \sum_{n=-5}^{5} \mathcal{C}_n\{s(t)\} \exp(\jmath 2\pi n f_0 t)$. The $n$-th complex coefficient of the Fourier series was evaluated as: $\mathcal{C}_n\{s(t)\} := \frac{f_0}{N_{cyc}} \int_0^{\frac{N_{cyc}}{f_0}} s(t) \exp(-\jmath 2\pi n f_0 t)\, dt$ where $\jmath = \sqrt{-1}$ is the imaginary constant.

For each specific driving frequency and amplitude of the commanded current, we evaluated the transfer function $H_{e_R}$ as $H_{e_R}(f_0, I_c) = \frac{\mathcal{C}_1\{F_R^{f_0,I_c}(t)\}}{\mathcal{C}_1\{i_R^{f_0,I_c}(t)\}}$.

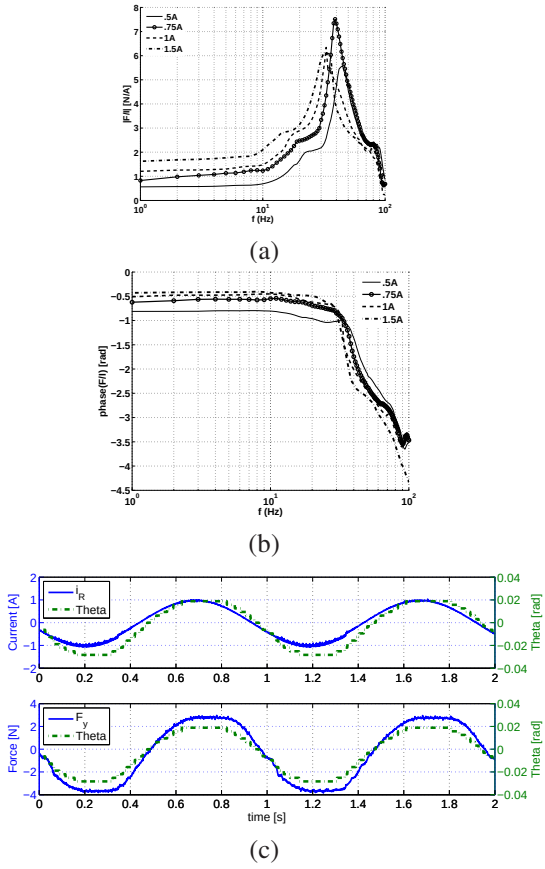


Fig. 2: Force transmission bandwidth. (a) Magnitude plot. (b) Phase plot. (c) Time plots of current ($i_R$), shaft angle ($\theta$) and transmitted force (component $F_y$). A delay can be noticed between $i_R$ and $\theta$ but not between $F_y$ and $\theta$. This delay is also related to the phase response at low frequencies.

Figures 2 (a) and (b) illustrate the transfer function of our device in terms of magnitude and phase plots respectively. The resonance frequency of about $30Hz$ can be considered enough for human interaction. The phase plot highlights a delay at low frequency that is due to the static friction of the DC motor. Indeed, at low frequencies such delay reduces with the amplitude of the input current because the static friction barrier can be overcome in a shorter time. Figure 2 (c) shows that while the motor current and the angular position are out of phase, the force at the end-effector follows the angular displacement without delay.

### B. Z-widths and haptic rendering

We consider a visco-elastic virtual object rendered at the robot end-effector. The mechanical action ($\boldsymbol{F}$) of the virtual object is translated into motor torques $\boldsymbol{\tau}$ via the Jacobian matrix:

$$\boldsymbol{\tau} = \boldsymbol{J}^T \boldsymbol{F} = \boldsymbol{J}^T(\boldsymbol{K}(\boldsymbol{p}_{des} - \boldsymbol{p}) - \boldsymbol{B}\dot{\boldsymbol{p}}) \tag{4}$$

Rendering large values of the stiffness and/or damping is challenging as the system might incur in instability due to delayed response and/or saturation [15].

In our current implementation, we run a real-time control platform (dSPACE, Germany) at $1KHz$ sampling frequency to read the position of the handle via the primary encoders (Faulhaber 5540) from the motors. The actuators are controlled in current (the desired torque is converted into desired current through the motor constant) via commercial servos (Ocarina Elmo Motion Control) providing a maximum output current of $5A$.

The stability test consisted in a double nested loop that was used to gradually increase the controller gains and find the combination between the maximum values of stiffness ($\boldsymbol{K}$) and damping ($\boldsymbol{B}$) for which the system still results in a stable response to a position input ($\boldsymbol{p}_{des}$ in (4)) [17]. The incremental limit of the gains were chosen from $100\frac{N}{m}$ to $4000\frac{N}{m}$ for $\boldsymbol{K}$ and from $0\frac{Ns}{m}$ to $5\frac{Ns}{m}$ for the damping $\boldsymbol{B}$.

Each trial was performed for a given value of stiffness and damping: a desired displacement $\boldsymbol{p}_{des}$ ( with $\parallel \boldsymbol{p}_{des} \parallel = 2[cm]$) was input to the controller and the step response of the system was observed. Instability of the system for a combination of stiffness and damping values was considered as the one producing end-effector oscillations for more than 0.3 seconds or saturation of the motor drivers. The procedure was repeated by gradually incrementing K until instability occurs. Then the the damping B was incremented and the stiffness K internal loop was restarted with the smallest stiffness coefficient ($100\frac{N}{m}$).

In order to investigate any anisotropy of the system, the Z-width test was performed along three different directions: *X-displacement* were motors rotate in phase, *XY-displacement* (or diagonal displacement) were only one motor produces the required displacement and *Y-displacement* were motors rotate in anti-phase. Stability regions are shown in Fig.3. Note that during the x-displacement the inertia of the system is less than in the other two directions (see Sec. III-C) hence, for low damping gains ($< 1\frac{Ns}{m}$) higher $\boldsymbol{K}$ gain can be achieved.

### C. Perceived Impedance

For our device, the inertial tensor can be easily derived from the kinetic energy ($T$) of the system.

Moving masses, pulleys and rotors' inertia contribute to the kinetic energy of the system. Before entering into mathematical details it is better to highlight some considerations and introduce the nomenclature that will be used in the mathematical model. As shown in Figure 1 the robot is symmetric and in the following we will split the inertia contributions into *left actuation* (LA) due to the action of the left motor and *right actuation* (LR) due to the action of the right motor. Moving masses will be rather split into $x$ and $y$ Cartesian actuation, $M_x$ and $M_y$ respectively.

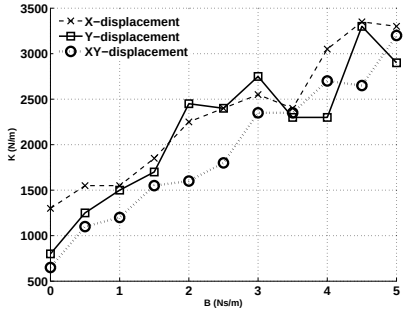


Fig. 3: Stability curves for the impedance controller in (4)

The rotor of each motor is connected through a shaft to the respective driving pulley spinning at the same angular velocity of the rotor. Therefore we will consider the ensemble rotor, connecting shaft plus driving pulley as a single system with equivalent inertia $I_{lm}$ and $I_{rm}$ for the left and right motor respectively. The motor torques are transmitted to the handle through a cable winded on eight identical (same radius and weight) idler pulleys. Four of these pulleys are fixed to the corners of the frame (see Figure 1) and therefore they only introduce inertia into the system. Of these four pulleys, the left couple rotates only in the presence of the left motor rotation and similar for the right couple of pulleys. We will refer to these inertial contribution as $I_{li}$ and $I_{ri}$ for the left and right couple respectively.

The remaining four pulleys do not rotate when the motors rotate at the same speed but not in phases (or when the handle is actuated only along the $y$ direction ). Therefore, their angular velocity is proportional to $\omega_L + \omega_R$. We indicate the equivalent inertia of these pulleys as $I_{mi}$ where *mi* stands for moving idler pulleys and highlight the fact that these pulleys rigidly move in the $y$ direction together with the handle.

Finally note that the eight idlers have a smaller radius compared to the driving pulleys and therefore their angular velocities must be scaled by the transmission ratio $\gamma$.

Regarding the moving masses, on the $x$ direction we only have the contribution of the handle, the load-cell and the connector to the slider. The $y$ direction is instead affected not only by these masses but also by the four moving pulleys and the horizontal slider.

With these considerations in mind we are now ready to derive the inertial tensor starting with the calculation of the kinetic energy $T$:

$$\begin{aligned} T = \frac{1}{2}(I_{lm}\omega_L^2 + I_{rm}\omega_R^2 + I_{li}\gamma^2\omega_L^2 + I_{ri}\gamma^2\omega_R^2 + \\ I_{mi}(\omega_R + \omega_R)^2 + M_x\dot{x}^2 + M_y\dot{y}^2) \end{aligned} \tag{5}$$

By grouping together the terms depending upon $\omega_L$ and $\omega_R$ the above expression can be rewritten as:

$$T = \frac{1}{2}(I_{LA}\omega_L^2 + I_{RA}\omega_R^2 + 2I_{mi}\omega_L\omega_R + M_x\dot{x}^2 + M_y\dot{y}^2) \tag{6}$$

where $I_{LA} = I_{lm} + I_{lp}\gamma^2 + I_{mi}\gamma^2$ is the contribution due the left actuation of the system and similar for $I_{RA}$.

The generalized inertia tensor $\boldsymbol{H}(\boldsymbol{p})$ can be computed from the kinetic energy by applying the Hessian operator:

$$\boldsymbol{H}(\boldsymbol{p}) = \begin{bmatrix} h_{xx} & h_{xy} \\ h_{yx} & h_{yy} \end{bmatrix} = \frac{\partial^2 T}{\partial^2 \dot{\boldsymbol{p}}} \tag{7}$$

Before applying the Hessian we convert the angular velocities into linear velocities along $x$ and $y$ through the forward kinematic in (1); We obtain: $h_{xx} = M_x + (I_{LA} + I_{RA} + 2I_{mp}\gamma^2)/r_m^2$, $h_{xy} = h_{yx} = (I_{LA} - I_{RA})/r_m^2$ and $h_{yy} = M_y + (I_{LA} + I_{RA} - 2I_{mp}\gamma^2)/r_m^2$ that does not depend on the robot position $\boldsymbol{p}$ (and is therefore homogeneous ) and leads to a perfectly diagonal matrix in the ideal case of perfect mechanical symmetry (i.e. $I_{LA} = I_{RA}$). With the aid of the CAD model (SOLIDWORKS 2013) we estimated the elements of the main diagonal as reported in Table II.

*1) Experimental estimation of damping and inertia tensors:* In the hypothesis that the driving cable is completely rigid and does not deform during interaction, the perceived mechanical impedance can be modeled with a linear system of second order differential equations:

$$\boldsymbol{F} = \boldsymbol{B}\dot{\boldsymbol{p}} + \boldsymbol{H}\ddot{\boldsymbol{p}} \tag{8}$$

where $\boldsymbol{F}$ is the bi-dimensional vector of forces ($F_x$ and $F_y$) acting at the robots' end-effector and $\dot{\boldsymbol{p}}$ and $\ddot{\boldsymbol{p}}$ are its velocities and accelerations respectively.

To estimate the matrix components $b_{ij}$ and $h_{ij}$ (respectively for $\boldsymbol{B}$ and $\boldsymbol{H}$ with imposed symmetry, i.e. $b_{12} = b_{21}$ and $h_{12} = h_{21}$) data was collected for five different end-effector positions (Center, North-East,North-West,South-East and South-West) according to the following procedure: for each of the five position, the robot's handle was manually moved with 10 seconds circular[1] (both clock-wise and counter-clock wise) displacements by a human operator and hand-handle interaction forces $\boldsymbol{F}_i$ and displacements $\boldsymbol{p}_i$ were recorded at $1000Hz$. Motors where electrically disconnected during the experiment to avoid effects due to the armature currents (e.g. the armature resistance of the motor would be perceived as extra damping, additional to the mechanical friction of the motor).

The spectral frequency of the perturbing forces was in all cases limited to $5Hz$.

Velocities and accelerations were obtained by backward differentiation of the displacement vector. However, due to the finite resolution (500 counts/rotation) of the encoders, before backward differentiation, both forces and displacements were forward and backward filtered (*filtfilt* Matlab function) with a low-pass 2nd order Butterworth filter with a $10Hz$ cutoff frequency.

The filtered forces together with the estimated velocities and accelerations were used for the regression (We used the multiple linear regression *mvregress* Matlab algorithm ). The

[1]a perfectly circular motion performed at uniform speed, would produce tangential velocities and centripetal accelerations of constant amplitude, i.e. uniformly rotating vectors describing perfect circles.

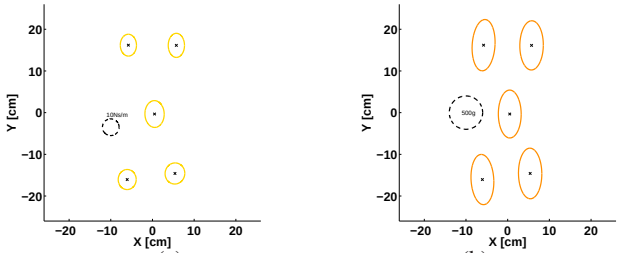


Fig. 4: Estimated damping (a) and inertia ellipses (b).

quantitative goodness-of-fitting (VAF) is shown in Table I for all five positions and the estimated tensors (for the central position of the workspace) are shown in Table II.

| | $C$ | N-E | N-W | S-E | S-W |
|---|---|---|---|---|---|
| VAF% | 96.6 | 98.1 | 97.8 | 98.2 | 98.4 |

TABLE I: Goodness-of-fit (VAF) for the five workspace positions: Central, North-East(N-E), North-West(N-W), South-East(S-E) and South-West(S-W) .

To better compare the estimated tensors among the five different positions, Figures 4(a) and (b) show the damping and inertia ellipses computed with the method proposed in [18].Unitary velocities and acceleration vectors are generated in Matlab and multiplied by the regressed tensor B and H respectively. The resulting force components are then drawn in the x-y plane. Therefore, the shape of each ellipse highlight the direction of maximal and minimal friction and inertia components. While the damping ellipses (or damping forces) are different for different workspace position, the experimental data show that the perceived inertia slightly change over the workspace and can be hence considered homogeneous.

| | $\boldsymbol{B}(Nm/s)$ | | $\boldsymbol{H}(Kg)$ | |
|---|---|---|---|---|
| Estimation Type | $B_{xx}$ $B_{yx}$ | $B_{xy}$ $B_{yy}$ | $I_{xx}$ $I_{yx}$ | $I_{xy}$ $I_{yy}$ |
| **CAD** | | | 0.5808 0 | 0 0.9295 |
| **MLR** | 11.5446 −0.0953 | −0.0953 16.0855 | 0.3422 −0.0016 | −0.0016 0.7176 |

TABLE II: Regressed coefficients for the friction and inertial tensors relative to the center of the workspace. Comparison is between the parameters obtained from the CAD model and those estimated with the Multiple Linear Regression (MLR).

## IV. CONCLUSIONS

This paper presents a novel haptic device that has been conceived in order to overcome the limitations of previously proposed designs. Our solution based on a H-shape cable-driven system provides a system that is homogeneous, light-weight and intrinsically safe. Several experiments have been conducted to assess the device performance in terms of force transmission bandwidth, Z-width and perceived impedance.

Apart from the homogeneity of the inertial tensor, the perceived inertia at the end-effector is particularly low when compared with well known planar robots such as the MIT-Manus [6]. In [21] it has been shown that the MIT-Manus presents a configuration dependent inertial tensor with a maximum mass of about 4.8 Kg, hence about seven times heavier than the H-Man (compare Tab II).

Due to its simplicity, in future the system can be controlled with a microcontroller instead of the dSPACE, hence providing a cost-effective solution for home-delivered rehabilitation therapy.

Another advantage of the platform is that it can be used in passive mode as it has been shown in [20] hence providing mechanical channels as a viable alternative to the haptic channels which require the use of motors and therefore increase system complexity and cost.

## REFERENCES


[1] Hayward, V., Astley, O. R., Cruz-Hernandez, M., Grant, D., Robles-De-La-Torre, G. (2004). Haptic interfaces and devices. Sensor Review, 24(1), 16-29.

[2] Westebring-Van Der Putten, E. P., Goossens, R. H. M., Jakimowicz, J. J., Dankelman, J. (2008). Haptics in minimally invasive surgery-a review. Minimally Invasive Therapy & Allied Technologies, 17(1), 3-16.

[3] Marchal-Crespo, Laura, and David J. Reinkensmeyer. "Review of control strategies for robotic movement training after neurologic injury." Journal of neuroengineering and rehabilitation 6.1 (2009): 20.

[4] Massie, T. H., Salisbury, J. K. (1994, November). The phantom haptic interface: A device for probing virtual objects. In Proceedings of the ASME winter annual meeting, symposium on haptic interfaces for virtual environment and teleoperator systems (Vol. 55, No. 1, pp. 295-300).

[5] Charnnarong, J., Hogan, N., Krebs, H. I., Sharon, A. (1995). U.S. Patent No. 5,466,213. Washington, DC: U.S. Patent and Trademark Office.

[6] Krebs, H. I., Hogan, N., Aisen, M. L.,Volpe, B. T. (1998). Robot-aided neurorehabilitation. Rehabilitation Engineering, IEEE Transactions on, 6(1), 75-87.

[7] Casadio, M., Sanguineti, V., Morasso, P. G., Arrichiello, V. (2006). Braccio di Ferro: a new haptic workstation for neuromotor rehabilitation. Technology and Health Care, 14(3), 123-142.

[8] Howard, I. S., Ingram, J. N., Wolpert, D. M. (2009). A modular planar robotic manipulandum with end-point torque control. Journal of neuroscience methods, 181(2), 199-211.

[9] S. Micera, M.C. Carrozza, E. Guglielmelli, G. Cappiello, F. Zaccone, C. Freschi, R. Colombo, A. Mazzone, C. Delconte, F. Pisano, G. Minuco, P. Dario (2005) A Simple Robotic System for Neurorehabilitation. Autonomous Robots19:271-284.

[10] D.J. Reinkensmeyer, L.E. Kahn, M. Averbuch, A. McKenna-Cole, B.D. Schmit, W.Z. Rymer (2000) Understanding and treating arm movement impairment after chronic brain injury: progress with the ARM guide, Journal of Rehabilitation Research and Development 37:653-662

[11] Zollo, Loredana, et al. "Design of a planar robotic machine for neuro-rehabilitation." Robotics and Automation, 2008. ICRA 2008. IEEE International Conference on. IEEE, 2008.

[12] Campolo, D., Accoto, D., Formica, D., Guglielmelli, E. (2009). Intrinsic constraints of neural origin: assessment and application to rehabilitation robotics. Robotics, IEEE Transactions on, 25(3), 492-501.

[13] Campolo, D., Formica, D., Guglielmelli, E., Keller, F. (2010). Kinematic analysis of the human wrist during pointing tasks. Experimental brain research, 201(3), 561-573.

[14] Tagliamonte, N. L., Formica, D., Scorcia, M., Campolo, D., Guglielmelli, E. (2010, October). Force control of a robot for wrist rehabilitation: Towards coping with human intrinsic constraints. In Intelligent Robots and Systems (IROS), 2010 IEEE/RSJ International Conference on (pp. 4384-4389). IEEE.

[15] Colgate, J. E., Brown, J. M. (1994, May). Factors affecting the z-width of a haptic display. In Robotics and Automation, 1994. Proceedings., 1994 IEEE International Conference on (pp. 3205-3210). IEEE.

[16] Weir, D. W., Colgate, J. E., Peshkin, M. A. (2008, March). Measuring and increasing z-width with active electrical damping. In Haptic interfaces for virtual environment and teleoperator systems, 2008. Haptics 2008. Symposium on (pp. 169-175). IEEE.

[17] Masia, L., Krebs, H. I., Cappa, P., Hogan, N. (2007). Design and characterization of hand module for whole-arm rehabilitation following stroke. Mechatronics, IEEE/ASME Transactions on, 12(4), 399-407.

[18] Mussa-Ivaldi, F. A., Hogan, N., Bizzi, E. (1985). Neural, mechanical, and geometric factors subserving arm posture in humans. The Journal of Neuroscience, 5(10), 2732-2743.

[19] Salisbury JK, Townsend WT (1993). Compact Cable Transmission with Cable Differential. U.S. Patent No. 5,207,114. Washington, DC: U.S. Patent and Trademark Office.

[20] Tommasino, P., Melendez-Calderon, A., Burdet, E., Campolo, D. (2014). Motor Adaptation with Passive Machines: a First Study on the Effect of Real and Virtual Stiffness. Computer Methods and Programs in Biomedicine. http://dx.doi.org/10.1016/j.cmpb.2013.12.019. (Article in press).

[21] Zollo, L., Accoto, D., Torchiani, F., Formica, D., Guglielmelli, E. (2008, May). Design of a planar robotic machine for neuro-rehabilitation. In Robotics and Automation, 2008. ICRA 2008. IEEE International Conference on (pp. 2031-2036). IEEE.